Advances in Water Resources 121 (2018) 446–455

Contents lists available at ScienceDirect

Advances in Water Resources

journal homepage: www.elsevier.com/locate/advwatres

In situ characterization of immiscible three-phase flow at the pore scale for a water-wet carbonate rock

Alessio Scanziani*, Kamaljit Singh, Tom Bultreys, Branko Bijeljic, Martin J. Blunt

Department of Earth Science and Engineering, Imperial College London, London, UK

ARTICLE INFO

Keywords:
Three-phase flow
Porous media
Wettability
X-ray imaging
Pore occupancy
Double displacement
Capillary trapping
Oil layers
Enhanced oil recovery
CCS

ABSTRACT

X-ray micro-tomography is used to image the pore-scale configurations of fluid in a rock saturated with three phases - brine, oil and gas - mimicking a subsurface reservoir, at high pressure and temperature. We determine pore occupancy during a displacement sequence that involves waterflooding, gas injection and water re-injection. In the water-wet sample considered, brine occupied the smallest pores, gas the biggest, while oil occupied pores of intermediate size and is displaced by both water and gas. Double displacement events have been observed, where gas displaces oil that displaces water or vice versa. The thickness of water and oil layers have been quantified, as have the contact angles between gas and oil, and oil and water. These results are used to explain the nature of trapping in three-phase flow, specifically how oil preferentially traps gas in the presence of water.

1. Introduction

Enhanced oil recovery (EOR) has been developed to increase oil production and meet the world's energy needs (Statoil, 2017). Among the EOR techniques currently employed, tertiary recovery with carbon dioxide (CO_2 -EOR) has been widely implemented, in both continuous and water alternating gas (WAG) injection strategies (Figuera et al., 2014; Leung et al., 2014). CO_2-EOR has the advantage of coupling the additional recovery of hydrocarbons with CO_2 geo-sequestration (or storage), CCS, which is an essential strategy to limit carbon dioxide emissions in the atmosphere and mitigate climate change (Global CCS institute, 2016; IEA, 2017; Kolster et al., 2017).

An accurate study of three-phase flow in porous media is crucial for the optimization of EOR and CCS. In these applications the three phases are: brine, already present in the reservoir and possibly flooded for secondary recovery purposes; oil, which can be at residual saturation if EOR is applied to depleted oil reservoirs; and a gas, which is injected to increase production as EOR. This third phase can be CO_2 as either gas or in a supercritical state, especially in CCS applications. Three-phase flow in porous media is also important for studies of NAPL (non-aqueous phase liquids) removal in unsaturated soils (Nakamura and Kikumoto, 2014).

Many previous studies of three-phase flow have focused on the measurement of relative permeabilities (Alizadeh and Piri, 2014), with steady-state experiments at the centimetre scale. Oak et al. (1990) obtained three-phase relative permeabilities of water, dodecane and nitrogen measuring saturations using X-ray absorption on a 7.6 cm long Berea sandstone core with 5 cm diameter. The relative permeabilities were obtained using Darcy's law and the pressure drop across the core. In a water-wet medium, the relative permeability of water (k_{rw}) was only a function of the water saturation (S_w). As the most wetting phase, it was hypothesized that water always occupies the narrowest regions of the pore space. Similarly, the gas relative permeability (k_{rg}) depended only on gas saturation (S_g), as it is was assumed to occupy the largest pores as the most non-wetting phase. The oil relative permeability (k_{ro}), in contrast, was a function of the saturation of the other phases. It is thought that the oil occupies pores of intermediate size (Blunt, 2017; Moghadasi et al., 2016; Ranaee et al., 2016). Di Carlo et al. (2000) performed similar experiments on sandpacks with different wettabilities, demonstrating how the arrangement of the three phases (pore occupancy and the existence of wetting layers) might affect the relative permeabilities. However, despite a large body of core-scale experimental measurements of three-phase flow, the pore occupancy has not been determined directly (Alizadeh and Piri, 2014).

To understand the pore-scale physics, Oren et al. (1992) visualized the remobilization of oil caused by the double drainage mechanism of gas displacing oil displacing water during gas injection from waterflood residual oil saturation in a two-dimensional (2D) micromodel. This was observed in a water-wet system where oil spreads spontaneously over the water while gas invades the centres of the pores, sandwiching the oil phase in layers that are gradually drained increasing the oil recovery. Keller et al. (1997) replicated the pore-space pattern of a Berea sandstone in a silicon wafer micromodel, and observed the formation of

* Corresponding author.
E-mail address: alessio.scanziani16@imperial.ac.uk (A. Scanziani).

https://doi.org/10.1016/j.advwatres.2018.09.010
Received 5 June 2018; Received in revised form 12 September 2018; Accepted 14 September 2018
Available online 21 September 2018

stable oil layers and the occurrence of both double drainage and double imbibition (water displacing oil displacing gas) events. Sohrabi et al. (2008, 2004); Sorbie and Dijke (2010) studied the behaviour of the three phases during WAG injection in 2D systems in which the wettability was altered, to determine recovery and pore occupancies for repeated cycles of water and gas injection.

These observations in micromodels allowed Van Dijke et al. to develop pore-scale network simulators of three-phase flow (Van Dijke et al., 2004; 2006) that can account for arbitrary wettability. In particular they modelled multiple displacement events, where one phase displaces another and so on, in a chain of arbitrary length (Van Dijke et al., 2004). Piri and Blunt (2005) developed another pore-network model representing immiscible three-phase flow, which computed relative permeabilities and capillary pressures using a random network representing the pore space of Berea sandstone, for different wettability conditions. More recently, improvements have been achieved with pore network models including multiple displacement and precise criteria for the formation and collapse of layers, based on thermodynamic constraints (Al-Dhahli et al., 2013; Zolfaghari and Piri, 2017a,b).

A reliable benchmark for pore-network simulators would be the direct visualization of three-phase flow in situ, i.e. inside the three-dimensional (3D) pore space, instead of 2D idealised micromodels. In the last decade, the advent of X-ray micro computed-tomography (μ-CT) has allowed the direct visualization of multiphase flow (Blunt et al., 2013). Images have been obtained for two-phase flow with both laboratory-based μ-CT scanners (Alhammadi et al., 2017; Herring et al., 2017) and at synchrotron sources, which enables the pore-scale dynamics to be captured with a time resolution of tens of seconds (Andrew et al., 2015; Reynolds et al., 2017; Schlüter et al., 2016; Singh et al., 2017).

A few authors have reported in situ studies of immiscible three-phase flow in porous rocks. Iglauer et al. (2013, 2014) obtained synchrotron and laboratory-based μ-CT images, at ambient conditions, of a Clashach sandstone saturated with brine, oil and gas to compare the effect of different displacement sequences on oil recovery and gas storage. They demonstrated that, for a water-wet system, gas injection in a virgin oil reservoir leads to lower residual oil saturations and higher gas trapping than when gas is injected after waterflooding. In the mixed-wet case studied in (Iglauer et al., 2014), however, this was not observed. Khishvand et al. (2016) applied a detailed analysis of high resolution two- and three-phase images of a Berea sandstone, at ambient temperature and a pressure of 5.52 MPa, to characterize multiple displacement events and relate them to the wettability state defined by local contact angles. Feali et al. (2012) investigated the role of oil layers, comparing a spreading system ($C_s > 0$, where $C_s = \sigma_{gw} - \sigma_{gw} - \sigma_{ow}$ is the spreading coefficient) with a non spreading one ($C_s < 0$). They showed that for $C_s > 0$ oil layers were present and a low oil saturation was reached, while if $C_s < 0$ the oil phase was disconnected, giving lower recovery.

In this work we use X-ray tomography to study three-phase flow in a carbonate rock at subsurface temperature and pressure conditions to quantitatively characterize: (a) pore occupancy, (b) multiple displacement processes, (c) wettability associated with spreading oil layers, and (d) trapping. To achieve this we design a sequence consisting of oil injection into a fully water-saturated pore space (OI), waterflooding (WF1), gas injection (GI) and second waterflooding (WF2).

3D images of the pore space saturated with three phases can be analysed with a maximal ball-based pore morphology analysis to quantify pore occupancy. In this paper we employ the maximal ball (MB) method (Bultreys et al., 2015). The largest sphere occupying the pore space are found from a dry scan of the sample (Dong and Blunt, 2009; Raeini et al., 2017), and these are compared to the grey scale images to obtain a relation between the dimension of the pores and the phase sitting in its centre. This 3D quantification of pore occupancy enables the validation of network model predictions of displacement processes (Bultreys et al., 2018; Van Dijke et al., 2004).

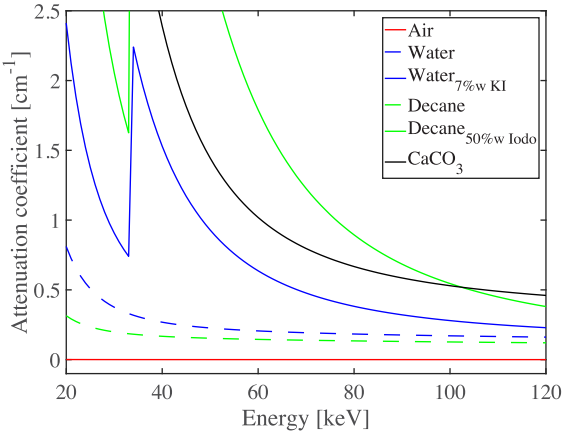

Fig. 1. Attenuation coefficients of different materials and mixtures. The selected materials are shown with solid lines. Blue, green, red and black are used respectively for brine, oil, gas and rock phases. (For interpretation of the references to colour in this figure legend, the reader is referred to the web version of this article.)

Along with the phase occupancy statistics, the monitoring of multiple displacements is crucial for accurate modelling of three-phase flow (Alizadeh and Piri, 2014; Van Dijke et al., 2004). We will obtain high-resolution images to visualize the multiple displacement mechanisms of double drainage and double imbibition, which has previously only been characterized in 2D micromodels (Keller et al., 1997).

Finally, we visualize the formation of spreading oil layers, in the presence of gas and water, allowing for an increase in oil recovery through their drainage (Alizadeh, 2014; Ranaee et al., 2015; Vizika and Lombard, 1996). These layers also influence the competition between snap-off and piston like displacement (Blunt, 2017), causing differences in trapping mechanisms between the two non-wetting phases (oil and gas).

Our study also provides quantitative information of the local thickness and connectivity of oil and water layers which, along with wettability characterization, is then used to interpret the degree of trapping. We determine if we have layers of sufficient thickness to contribute to hydrodynamic conductivity and displacement processes.

2. Materials and methods

2.1. Materials

A Ketton sample was selected as the rock for this study, with a mean diameter of 4.9 mm and a mean length of 19.5 mm. The porosity was measured to be 29.8% with a Helium porosimeter and 15.2% with image analysis on the micro-CT scans obtained in these studies. The difference between the two values is due to the presence of microporosity within the oolith grains, with pore dimensions lower than the resolution of the images, which is therefore not captured with traditional segmentation of the X-ray data. The composition of the rock is > 99% calcite (Andrew et al., 2014; Tanino and Blunt, 2012). The sample was cleaned with methanol to remove any impurities and dried in a vacuum oven at 95 °C for 24 hours (Kamaljit et al., 2016).

The selection of the fluid phases was driven by a trade-off between the aim of replicating a reservoir system whilst being able to distinguish between them in the X-ray images. Fig. 1 shows the X-ray attenuation coefficients for solid, aqueous, oil and gas phases with and without the addition of dopants (Khishvand et al., 2016; National Institute of Standards and Technology, 201). In the photon energy range we set in the micro-CT scanner (20–80 keV), the attenuations for pure gas, water and decane are quite similar, which would make unambiguous segmentation of the phases difficult. For this reason, different dopants were added to

Table 1
Thermophysical properties of the selected phases. Densities and viscosities are computed at experimental conditions (8MPa and 60 °C) from data provided in (National Institute of Standards and Technology, 201). Interfacial tensions are measured at 1.01 MPa and 289.15 K.

	Density [kg/m^3]	Viscosity [$\mu Pa \times s$]	Interfacial tension [mN/m]
Brine (H_2O + 7%w KI)	1052	1237	$\sigma_{ow} = 47$
Oil (Decane + 50%w Iododecane)	931.7	1752	$\sigma_{go} = 27$
Gas (N_2)	93.78	19.01	$\sigma_{gw} = 72$

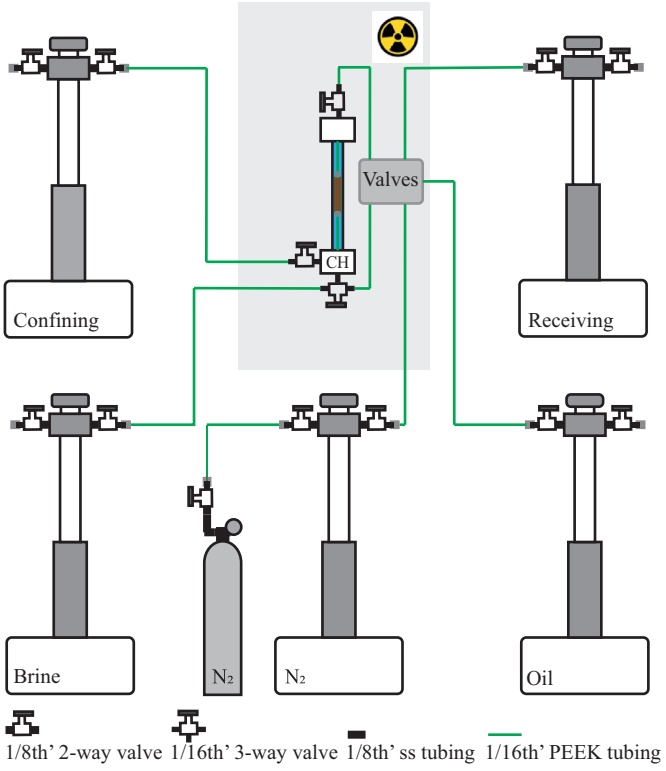

Fig. 2. Schematic of the flow loop used to perform the experiment. The grey shaded area represents the X-ray μ-CT enclosure. CH is the core holder (or flow cell).

both the water and the oil phase. A mixture with 7% by weight of potassium iodide (KI) in water was used as the brine phase, while a solution 50% by weight of iododecane in decane was used as the oil phase. The gas phase was chosen to be nitrogen, as it is fully immiscible with both oil and brine. The X-ray contrast between the doped phases has been judged with both contrast scans (Figure S1 in the Supplementary Information) and by inspection of the grey scale histograms (Figure S2 in the Supplementary Information). Table 1 lists the densities, viscosities and interfacial tensions of the phases used in the experiments. In this work we found no evidence that the wettability of the system changed on exposure to radiation as seen by (Brown et al., 2014): the laboratory instrument uses a relatively weak X-ray source and the contact angles we measure, see later, are consistent with measurements on undoped systems (Kamaljit et al., 2016).

2.2. Methods

2.2.1. Flow experiment

The flow experiment was performed using the flow loop shown in Fig. 2. Five pumps (Teledyne Isco, Lincoln, NE, USA) were used for confining, receiving and brine, oil and N_2 injection. A carbon fibre Hassler type flow cell was used to keep the rock under pressure with a confining fluid (water). The sample was placed in a Viton sleeve, and connected to the PEEK tubing of the hydraulic circuit with two steel end pieces. The flow cell was placed in a Zeiss Xradia 500 Versa 3D -CT scanner for image acquisition.

The sample was first flushed with carbon dioxide to remove all the air from the pores, then 100 pore volumes of brine with a flow rate of 0.1 mL/min were injected to ensure 100% water saturation. The pressure of the brine inside the sample was then raised to experimental conditions (8 MPa), with a confining pressure of 9.5 MPa, to fully insulate the sample and prevent any bypass of the fluid along its walls (Kamaljit et al., 2016). The temperature of the sample was then raised to experimental conditions (60 °C) with an electric heater wrapped around the carbon fibre sleeve, and a thermocouple fixed in contact with the sample inside the Viton sleeve. A proportional-integral-derivative (PID) controller is used to ensure a constant temperature in the rock sample.

2.2.1.1. Flooding sequence. Four injections were performed to simulate the displacement sequence in a reservoir under capillary force dominated flow conditions. All the injections were performed with a flow rate of 0.015 mL/min. Firstly, oil was injected in the brine-saturated sample at the top of the flow cell (oil injection, OI) for 35 minutes, with a total volume corresponding to 5 pore volumes (PV). Then, the first waterflooding (WF1) was performed, simulating secondary recovery with water injection in the reservoir, for a total of 15 PV from the bottom of the sample. The third and fourth floods were respectively gas injection (GI) from the top and second water injection (WF2) from the bottom, both of them for a total of 5 PV; these simulate a tertiary recovery strategy. Details about the injections, including values of capillary number (which were always in the capillary dominated regime) are provided in Table 2.

2.2.2. Imaging

Scans with two different resolutions were acquired after each injection: first, a 0.4× magnification lens was employed at the detector, to maximize the field of view, and the relative position of source and detector was set to have a resolution of 5 μm per voxel side. Then, two scans were performed with a lens with 4× magnification, to obtain high resolution images, for a smaller field of view, with 2 μm per voxel side.

The low resolution scan was built by stitching together 4 separate scans at different heights (Fig. 3), to obtain an image of almost the whole sample, with dimensions larger than the elementary representative volume, to measure saturations and connectivity. The high resolution scans were performed at two locations at the mid-bottom and mid-top of the rock, to investigate the pore-scale mechanisms of trapping and to measure contact angle. The high resolution images required more projections and longer exposure time, as shown in Table 2. After OI, we increased both the number of projections and the exposure time for the following scans, to obtain higher quality images for WF1, GI and WF2.

2.2.3. Image processing

The reconstruction of the X-ray images was performed with the software included in the Zeiss Versa 500 micro-CT, which allows corrections for centre shift and beam hardening (Andrew et al., 2014). The 5 μm resolution images were stitched together, taking advantage of the wide overlapping region between each scan (at least 25% of the whole height of each scanned image, Fig. 3). All the images were registered using the

Table 2
Details of the experimental procedure. The capillary number is computed as $Ca = \sigma q/\mu$ where the interfacial tension (σ) and the viscosity of the injecting phase (μ) are shown in Table 1, while the Darcy velocity q is computed dividing the flow rate by the sample cross section. The number of projections and the exposure time for both images with low (LR) and high resolution (HR) were increased after OI, to increase the image quality.

	Flow rate [mL/min]	Capillary number	PV	N projections (LR - HR)	Exposure time (LR - HR) [s]
Dry	-	-	-	2400 - 4000	1.5 - 1.7
OI	0.015	4.4×10^{-7}	5	2400 - 4000	1.5 - 1.7
WF1	0.015	3.1×10^{-7}	15	3000 - 6000	1.7 - 1.9
GI	0.015	8.5×10^{-9}	5	3000 - 6000	1.7 - 1.9
WF2	0.015	3.1×10^{-7}	5	3000 - 6000	1.7 - 1.9

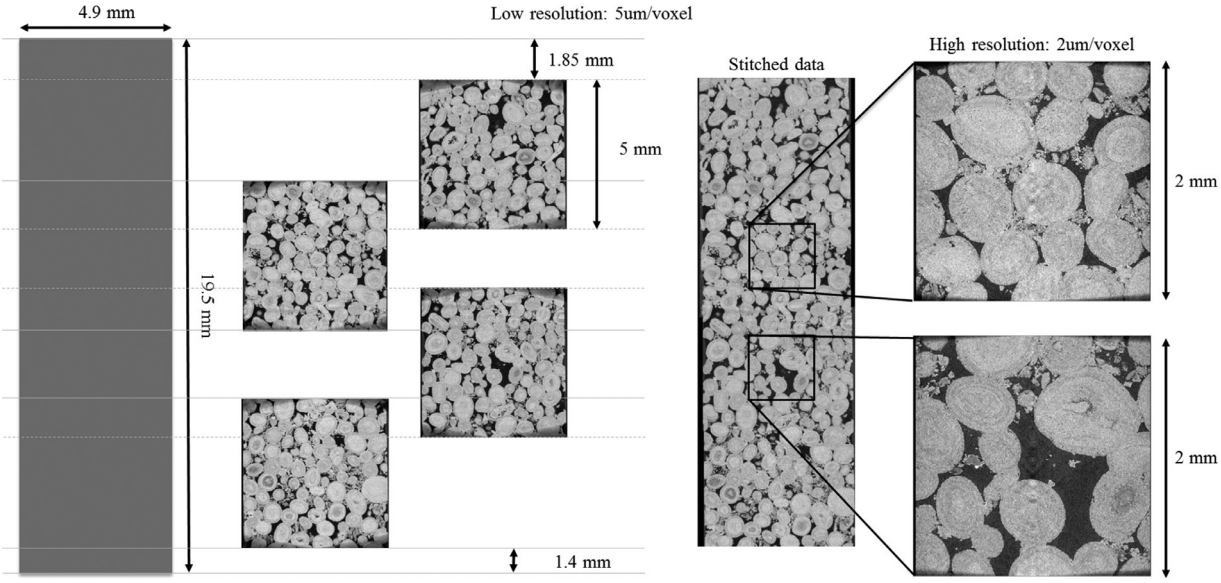

Fig. 3. Location and dimension of the low and high resolution scans. The images of the rock shown here are the low- and high-resolution dry scans.

dry scan as a reference, allowing direct comparison after each injection step. A non-local means edge-preserving filter was applied to smooth the grey scale images and improve watershed segmentation (Buades et al., 2008). The non-local means filter assigns to each voxel the weighted average of the grey scale values of the n voxels in the neighbourhood of the selected one. The similarity value is the weight used in the averaging procedure, and the lower it is, the less the images are smoothed.

The segmentation of the lower resolution images was performed using a watershed method with the possibility of selecting different gradient values for different phases (*2D-histogram segmentation* function of Avizo (Jones et al., 2007)). The seeded watershed segmentation algorithm first searches for the seeds of the three phases, i.e. the portions of the pore space where the high certainty exists about the phase present, which are far from the interfaces. These seeds are then grown proportionally to a certain gradient value until all the voxels of the image are assigned to some phase. The advantage of this algorithm is that it preserves the continuity of the phases with acceptable accuracy (Schlüter et al., 2014). However, the shape of the interface between the phases, which is important for computing quantities such as contact angles and curvature, is affected by uncertainties and may be altered by the filtering procedure (Alhammadi et al., 2017). When dealing with the high resolution images, the WEKA machine learning segmentation method (Arganda-Carreras et al., 2017) was applied using Image J software on non-filtered images, obtaining higher quality results, especially when considering small details at the interfaces. However, WEKA is much more CPU intensive than watershed segmentation and it was not possible to apply it to the bigger dataset at lower resolution.

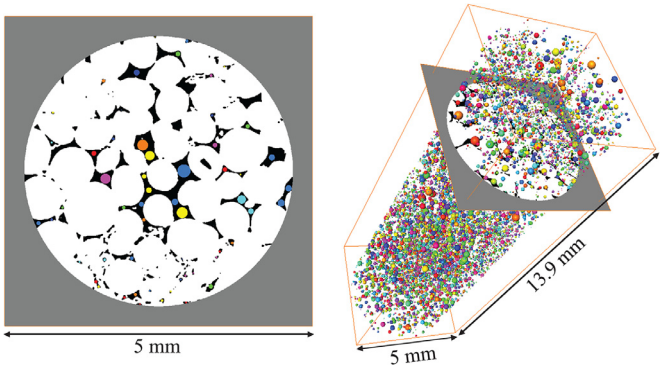

Fig. 4. Pore centres are defined by maximal balls in the largest regions of the pore space, using the dry segmented images (on the left), where black is the pore space, white the rock phase and the maximum balls are coloured with different labels. On the right, a 3D visualization of the spheres along the whole micro core is shown. Different colours are assigned to different spheres representing individual pores.

2.2.4. Pore occupancy

To analyse the pore occupancy, we identified local dilations and constrictions in the pore space using the maximal ball method as a part of generalized network extraction algorithm of (Raeini et al., 2017) to obtain the description of the pore space shown in Fig. 4. The diameter of the maximal ball is considered to be the pore diameter.

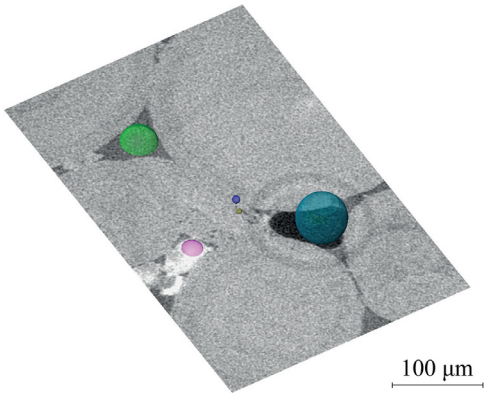

Fig. 5. Example of maximal balls (semi-transparent) inside the pore space (slice of grey scale 3D data). The grey scale values of the voxels inside the spheres are averaged to identify pore occupancies.

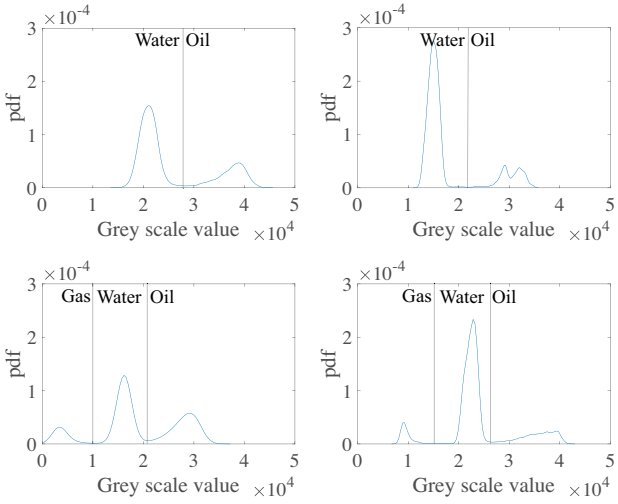

Fig. 6. Histograms of grey scale probability density functions (pdf) obtained after averaging the grey scale values inside the maximal balls on images after oil injection (OI, top-left), first waterflooding (WF1, top-right), gas injection (GI, bottom-left) and second waterflooding (WF2, bottom-right). To assign the pores to water, oil or gas, the minima of the pdf functions are identified (vertical grey lines).

The spheres representing the pores (local dilations in the pore space) are superimposed on grey scale wet images, for each of the injection steps, as shown in Fig. 5 (Bultreys et al., 2018). The mean grey scale value associated to the voxels inside each sphere (refer to Fig. 5) is computed. This results in a distribution of mean grey scale values where, due to the averaging over the voxels in each sphere, the grey scale probability distribution clearly identifies different peaks, corresponding to the different phases. The grey scale thresholds classifying the phases are set as the minima in the probability density functions, as shown in Fig. 6. With this procedure the pore centres were segmented into those where brine, oil or gas resides. As shown in the Supplementary Information (Figure S3), the centre of each pore, defined by the spheres, always corresponds to one phase only, as the oil and water layers, even when they are thicker (after first and second waterflooding), do not reach the centre of the pore.

3. Results and discussion

In Section 3.1, we first present the saturation of the three phases in the volume imaged with the low-resolution scan, after each displacement step. Then, in Sections 3.2, 3.3 and 3.4 we respectively show (i) a characterization of three-phase displacements in terms of pore size and pore occupancy, (ii) a 3D visualization of double displacement mechanisms, namely double drainage and double imbibition, and (iii) a detailed description of contact angles, oil layer formation and trapping mechanisms in a high resolution image.

Saturations and pore occupancy were computed on 5 µm resolution images of a large part of the rock sample (Fig. 7), increasing the statistical significance of these results. For the detailed characterization of pore-scale phenomena of double displacements, oil layer formation, trapping mechanisms and contact angle measurements, we relied on the dataset with higher resolution (Fig. 8).

3.1. Saturations

The saturation of the phases after each step was quantified from the segmented images by the ratio of the voxels assigned to the selected material to the total number of voxels assigned to the pore space. The saturation points at the end of each injection are shown in the ternary diagram in Fig. 9, with the distribution of the phases shown in Fig. 10. Starting with the core fully saturated with water, oil was injected (OI, green arrow in Fig. 9); the water and oil saturation after OI were 37.6% and 62.4% respectively. Then, WF1 (blue arrow in Fig. 9) allowed production of oil and final saturations of 48.0% and 52.0% for water and oil were measured; the oil recovery with water injection was 17%, which is lower than previous studies on similar systems (Kamaljit et al., 2016). The reason for this is that not all the oil was trapped at the end of WF1. As evident in Fig. 10, there is a large cluster of oil connected to the outlet that could be partially displaced on further water injection. The third injection introduced gas in the sample (GI, red arrow in Fig. 9); this allowed for a production of both water and oil with saturations of 4.0%, 30.5% and 65.5% for water, oil and gas respectively at the end of the GI step; at this point, the oil recovery, with respect to initial oil saturation, was 51%. The last step was the second waterflooding (WF2, blue arrow in Fig. 9), allowing for gas trapping and further oil recovery: the final saturations were 28.6%, 18.6% and 52.8% for water, oil and gas respectively and the recovery factor was 70% with respect to the initial oil saturation.

These results show how the injection of gas after waterflooding, and possibly another injection of water, may significantly increase oil recovery. Gas injection displaced connected oil, but also led to the rearrangement of disconnected oil clusters and their partial production, as evident in Fig. 10. Further evidence for the displacement of trapped oil is provided later in the paper.

3.2. Pore occupancy

Using the procedure described in Section 2.2.4, the pore centres identified by maximum ball spheres were assigned to the three phases.

We obtained bar graphs approximating the probability density functions of the pore sizes occupied by each phase, Fig. 11: the heights f_i^α of the bars were obtained as follows:

$$f_i^\alpha = \frac{N_i^\alpha}{N_i} \tag{1}$$

where N_i^α is the number of pores associated with the phase α for each i-th bin, while N_i is the total number of pores in each i-th bin.

From the results shown in Fig. 11 we can see that, as expected in a water-wet system, during OI oil invaded the largest pores, while water remained confined in the smaller ones. With WF1, oil is pushed away from some medium/small-sized pores, replaced by water and produced. During GI, gas is the most non-wetting phase and invades the centre of the larger pores, while oil and water are squeezed into smaller pores. A noticeable movement of oil happens during gas injection: it is displaced by gas, which replaces oil in the centre of the larger pores. The oil that was trapped during WF1 is as a consequence reconnected in cavities smaller than those occupied before and it is produced. Some connected

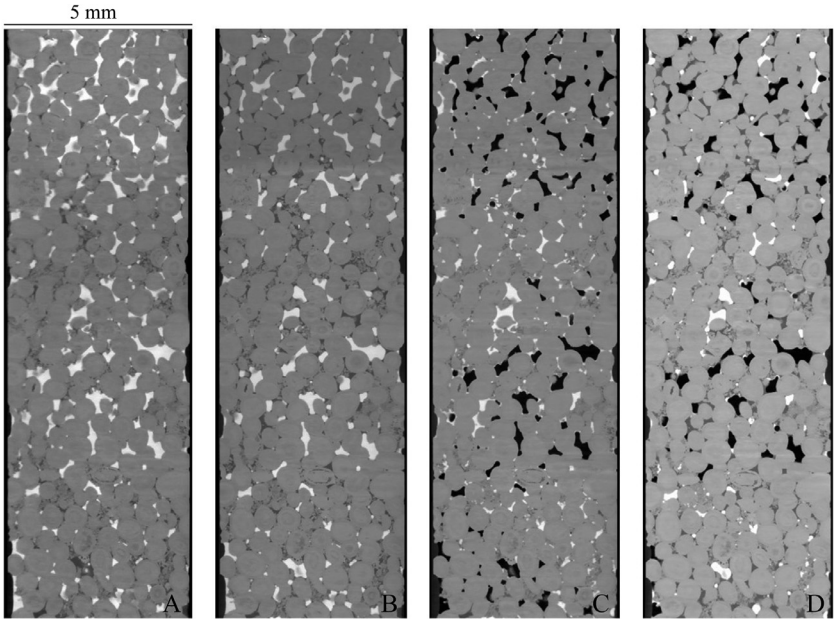

Fig. 7. 5 μm resolution filtered wet images of the Ketton sample after oil injection (A), first waterflooding (B), gas injection (C) and second waterflooding (D). Due to their different X-ray attenuation coefficients, the four phases result in increasing grey scale values with the darkest being gas phase, followed by brine, rock and oil as the brightest one.

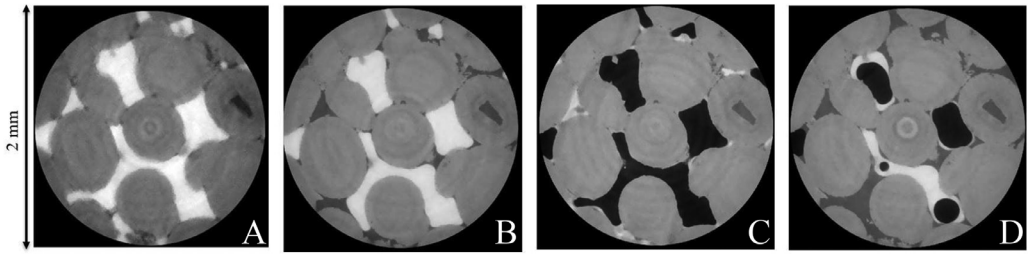

Fig. 8. 2 μm resolution filtered wet images of the Ketton micro sample after oil injection (A) first waterflooding (B), gas injection (C) and secondary waterflooding (D). Due to their different X-ray attenuation coefficients, the four phases result in increasing grey scale values with the darker gas phase, followed by brine, rock and oil as the brightest one.

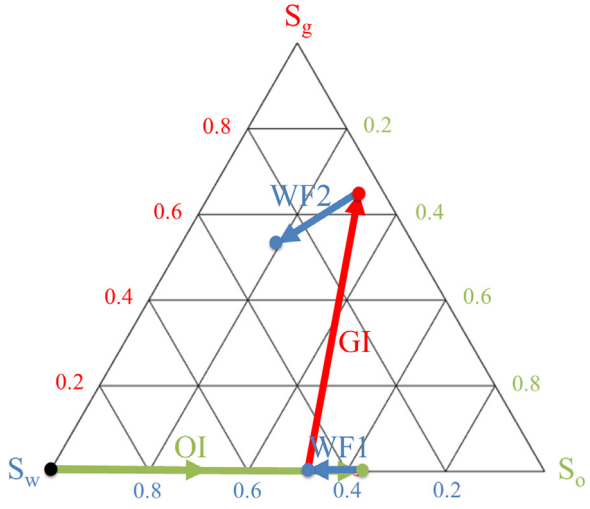

Fig. 9. Three-phase diagram showing the sequence of displacement processes and the end-point saturations. The core is at first fully saturated with water (black point at bottom left of the diagram), then oil is injected during oil injection (green arrow) until the green point; the first waterflooding is represented by a blue arrow and then gas injection and second waterflooding with red and blue arrows and end points. (For interpretation of the references to colour in this figure legend, the reader is referred to the web version of this article.)

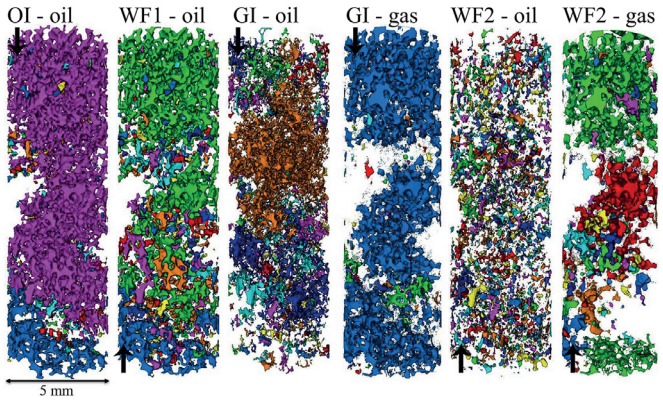

Fig. 10. 3D representation of the connectivity of oil and gas phases after oil injection (OI), first waterflooding (WF1), gas injection (GI) and second waterflooding (WF2). Each column represents only one phase and different colours indicate disconnected clusters of the selected phase. The black arrows indicate the direction of the injection for each step.

oil is also likely directly displaced by gas. WF2 causes both a further production of oil, which drains in layers, along with trapping of the gas phase, both inside layers of oil and surrounded only by water.

The results shown in Fig. 11 agree with our current understanding of three-phase flow in a water-wet medium (Blunt, 2017): water, oil and gas occupy respectively small-, medium- and larger-sized pores. How-

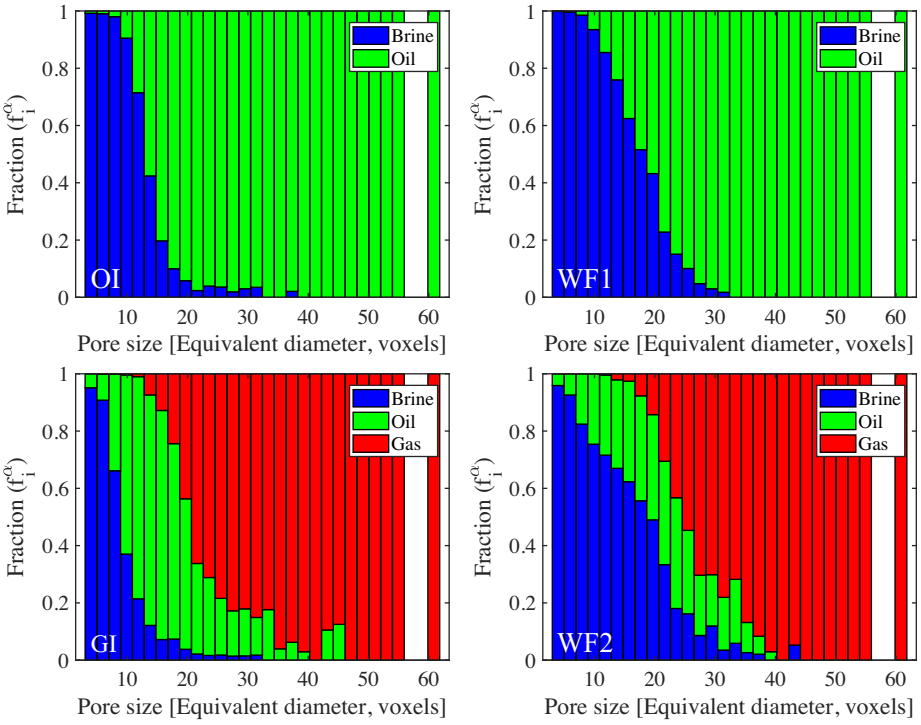

Fig. 11. Bar graphs representing the pore occupancy. Each coloured bar represents the fraction of the pores with an inscribed maximum ball with a diameter in the bin range occupied by brine, oil and gas.

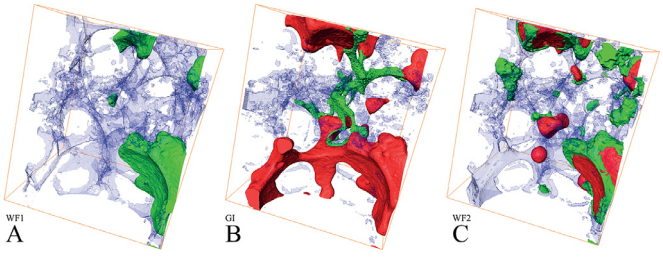

Fig. 12. 3D representation of a selected 1×1×1 mm^3 sub-volume of the pore space, showing how oil, which is disconnected after WF1 (A), is reconnected with GI (B) and then trapped in layer surrounding the gas phase after WF2 (C). Oil and gas are respectively green and red, while the brine phase is represented in semi-transparent blue. The rock phase has been rendered transparent in all images. (For interpretation of the references to colour in this figure legend, the reader is referred to the web version of this article.)

ever, there is some spreading in the thresholds between pores occupied by different phases, instead of a sharp demarcation. There can be some small pores still occupied by oil, and intermediate ones where water and gas are present. Pore filling, in fact, is not only driven by the dimension of the pores, but other factors have an influence as well, such as connectivity, cooperative pore filling (Blunt, 2017) and variations in local contact angles (Alhammadi et al., 2017; AlRatrout et al., 2017).

3.3. Double drainage and double imbibition

The high resolution images allowed detailed 3D rendering of the segmented data, and the visualization of pore-scale phenomena such as double displacement mechanisms. After WF1, some oil was trapped in the pore space (Fig. 12A), surrounded by water. With the injection of gas, gas displaced water and, when it could contact oil, it directly displaced oil, as they compete for the space in the centre of the larger pores. Mass conservation hence constrains oil to move towards the medium-sized pores, occupied by water (Fig. 12B). This gas-displacing-oil-displacing-water is a double displacement mechanism called double drainage as both gas and oil are non-wetting phases (Oren et al., 1992). With WF2, we observed the opposite mechanism: injected brine, being the most wetting phase, reconnected through the small and medium pores. However, since these were partially occupied by oil, the latter is mobilized again: it was pushed towards larger pores, and subsequently part of it is produced and part surrounded gas, trapping the latter (Fig. 12C). This double displacement is called double imbibition as the two most wetting phases are driving the invasion of the pore space. These double displacement mechanisms have a strong influence on the dynamics of three-phase flow (Van Dijke et al., 2004), and future work will involve a detailed characterization of these phenomena to benchmark and improve pore-scale models.

3.4. Contact angles, spreading oil layers and trapping

The value of the effective contact angle between oil and water after waterflooding is recognised as a direct measure of the wettability of the system (AlRatrout et al., 2017; Andrew et al., 2014; Blunt, 2017; Jafari and Jung, 2017; Khishvand et al., 2016; Scanziani et al., 2017). This effective contact angle is different than the intrinsic one measured on a smooth surface (Rabbani et al., 2017). We have selected a subvolume of the pore space, illustrated in Fig. 13, and performed the automatic estimation of contact angle developed by Scanziani et al. (2017) on the images after WF1 (Fig. 13B). This method measures the contact angle on the segmented images by fitting a curve to the interface between the fluids using the physical constraint of constant curvature given by the Young-Laplace law when the fluids are in equilibrium. The result is illustrated in Fig. 14 which shows a distribution of contact angles, measured through the water phase at 3139 points, around a mean value of 47.5 degrees, with a standard deviation of 19.1 degrees. This result is in line with those found in literature for similar systems (Kamaljit et al., 2016; Scanziani et al., 2017) and confirms a weakly water-wet behaviour, coherent with the results of pore occupancy illustrated in

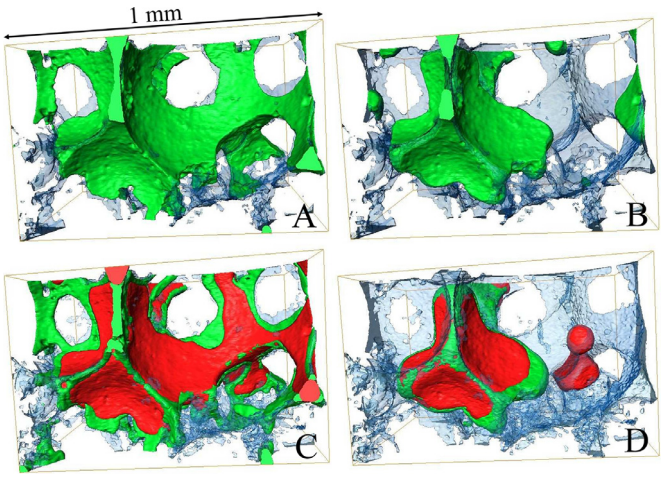

Fig. 13. 3D representation of a subvolume of the pore space with rectangular cross section, showing the occupancy of two pores where we observed different trapping mechanisms for oil and gas phases. Oil is green, gas red and water semi-transparent blue, with the rock phase rendered transparent. The four panels represent (A) oil injection, (B) first waterflooding, (C) gas injection and (D) secondary waterflooding. (For interpretation of the references to colour in this figure legend, the reader is referred to the web version of this article.)

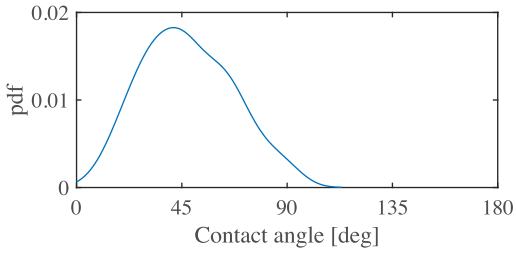

Fig. 14. Probability density function (pdf) distribution of the oil-water contact angle measured through the water after first waterflooding for the subset shown in Fig. 13B.

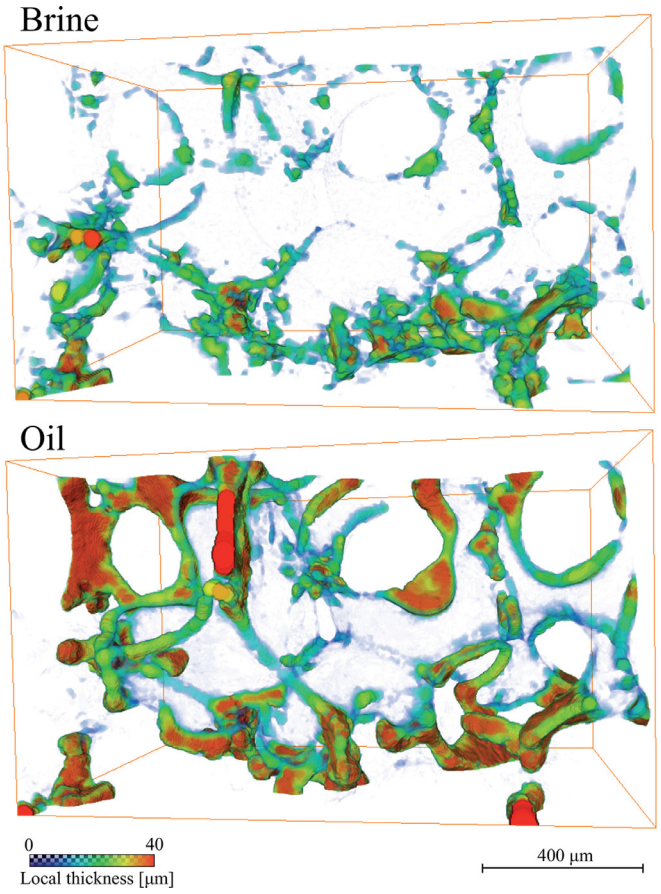

Fig. 15. The local thickness of the water and oil layers was computed for the subset shown in figure 13: the water and oil phase were isolated and maximal balls were inscribed in their structure for both the datasets after WF1 (in the case of water) and after GI (in the case of oil).

Section 3.2. The distribution of contact angle - instead of a unique value - is a consequence of a variation, in the selected domain, of sub-resolution features such as roughness and pore geometry (Andrew et al., 2014).

From Table 1, the spreading coefficient is - 2 mN/m, which is close to zero: we do see the presence of oil layers throughout the pore space when gas and water are present, see Fig. 13C and D. Therefore we assume that the effective gas-oil contact angle is close to zero: in our images we were unable to determine clear contacts between gas, oil and the solid, which again is consistent with the presence of oil layers. It is difficult to measure the gas-water contact angle directly, as oil layers prevent frequent direct contacts of water with gas. However, this could be estimated using the Bartell-Osterhof relation (Bartell and Osterhof, 1927; Blunt, 2001). Panel C of Fig. 13 refers to the system after gas injection. The oil is sandwiched in spreading layers in the corners of the pore space. The thickness of these spreading layers was measured fitting maximum spheres to the structures (Hildebrand and Ruegsegger, 1997) - a 3D map of their thickness is provided in Fig. 15.

During an imbibition process, capillary dominated flow in the pores is regulated by the competition between snap-off and piston-like displacement (Blunt, 2017). This competition is controlled by the aspect ratio or the relative dimension of adjacent pores and throats, the geometry of the pore space, the connectivity, the flow rate and the wettability.

Fig. 13 illustrates two different imbibition processes: single brine-displacing-oil imbibition during WF1 (panel A to panel B); and double brine-displacing-oil-displacing-gas imbibition during WF2 (panel C to panel D). These two phenomena took place in the very same pore space, with very similar capillary numbers, hence the main difference in the competition between snap-off and piston-like displacement is given by the contact angle between the displaced and injected phases. For lower contact angles, snap-off and trapping are more favoured. During the single imbibition, where water displaces oil, the oil-water angle has been measured to indicate only weakly water-wet conditions (Fig. 14), and piston-like displacement is favoured. In contrast, the double imbibition process during WF2 leads to a snapped-off ganglion of gas. Hence, gas trapping by oil is preferred over oil trapping by water in the same pores.

This behaviour has been observed indirectly on measurements in sand packs of the amount of gas trapped by water alone, oil trapped by water alone, and gas trapped when oil is present at low saturation (Amaechi et al., 2014). More gas was trapped under three-phase conditions (in the presence of oil and water). The pore-scale interpretation of this, confirmed by our observations, is the following: due to the simultaneous presence of three phases, causing the formation of oil spreading layers, oil is strongly wetting to gas, with a contact angle close to zero. This favours snap-off, whereas if oil is trapped by water, the contact angle is higher and piston-like advance is more favoured. This explains that oil layers, in addition to allowing oil reconnection and production, also influence and increase the amount of gas trapping, facilitating the potential storage of carbon dioxide when this gas is used for tertiary oil recovery.

Fig. 15 provides a comparison between the thickness of brine layers after WF1 and oil layers after GI. In general the oil spreading layers are thicker and more pervasive than the wetting brine ones, which are confined to the narrowest corners of the pore space. Oil layer maps may be used in future for computing their permeability and to estimate the

velocity of oil flow through them and hence the oil relative permeability. In any event, the water and oil layers thicknesses are of the order of 10 μm or larger and are connected over the mm-scale, which is sufficient to contribute significantly to the phase conductance and displacement processes (Blunt, 2017).

4. Conclusions and future work

In this paper, we have developed a methodology to obtain a detailed 3D pore scale in situ analysis of immiscible three-phase flow at elevated temperatures and pressures, with a focus on pore occupancy, double displacement mechanisms, and the influence of water and oil layer thickness and wettability on non-wetting phase snap-off and trapping. The three phases were injected in the rock, initially fully saturated with brine, in this order: (i) oil injection (OI), first waterflooding (WF1), gas injection (GI) and second waterflooding (WF2). The quality of the images allowed us to have detailed insight of the pore-scale phenomena, and in particular:

1. We quantified the saturation after each injection step, describing the increase in oil recovery due to its remobilization via GI followed by WF2, with a behaviour similar to that previously observed (Feali et al., 2012; Iglauer et al., 2013).
2. We obtained a statistical representation of pore occupancy, which is crucial for obtaining improvements in existing three-phase network models. Water resides in the smallest pores and gas in the largest ones (Blunt, 2017). The pore sizes filled with oil, the intermediate-wet phase, depends on the amounts of oil and gas present.
3. Double drainage and double imbibition, previously observed in micromodels (Keller et al., 1997; Oren et al., 1992), have been imaged and described in 3D pore structures of carbonate rock.
4. We have shown how contact angle and fluid distribution play a role in the competition between piston-like displacement and snap-off leading to preferential trapping of gas in the presence of oil layers, as previously observed in sandpacks (Amaechi et al., 2014).
5. We obtained quantitative maps of the local water and oil layer thickness, which indicate that they are sufficiently thick to contribute to flow and displacement.

Future work could look at mixed-wet conditions and the resultant pore occupancies to test the theoretical predictions of Van Dijke and Sorbie (2002). Furthermore, different rocks and flooding sequences could be studied. These experiments could serve as benchmarks for quantitative comparison with and testing of pore-scale modelling tools.

5. Data availability

The raw and segmented 3D images of the rock after each injection are available at the Digital Rock portal (Scanziani, 2018).

Aknowledgments

We acknowledge Abu Dhabi National Oil Company (ADNOC) and Abu Dhabi Company for Onshore Petroleum Operations Ltd. (ADCO) for financial support.

Supplementary material

Supplementary material associated with this article can be found, in the online version, at doi:10.1016/j.advwatres.2018.09.010.

References

Al-Dhahli, A., van Dijke, M.I., Geiger, S., 2013. Accurate modelling of pore-Scale films and layers for three-Phase flow processes in clastic and carbonate rocks with arbitrary wettability. Transp Porous Media 98 (2), 259–286.
Alhammadi, A.M., AlRatrout, A., Singh, K., Bijeljic, B., Blunt, M.J., 2017. In situ characterization of mixed-wettability in a reservoir rock at subsurface conditions. Sci Rep 7 (1), 10753.
Alizadeh, A.H., 2014. The effect of saturation history on three-phase relative permeability: an experimental study. Water Resour Res (50) 1636–1664.
Alizadeh, A.H., Piri, M., 2014. Three-phase flow in porous media: a review of experimental studies on relative permeability. Rev Geophys 52 (3), 468–521.
AlRatrout, A., Raeini, A.Q., Bijeljic, B., Blunt, M.J., 2017. Automatic measurement of contact angle in pore-space images. Adv Water Resour 109, 158–169.
Amaechi, B., Iglauer, S., Pentland, C.H., Bijeljic, B., Blunt, M.J., 2014. An experimental study of three-Phase trapping in sand packs. Transp Porous Media 103 (3), 421–436.
Andrew, M.G., Bijeljic, B., Blunt, M.J., 2014. Pore-scale contact angle measurements at reservoir conditions using X-ray microtomography. Adv Water Resour 68, 24–31.
Andrew, M.G., Menke, H., Blunt, M.J., Bijeljic, B., 2015. The imaging of dynamic multiphase fluid flow using synchrotron-Based X-ray microtomography at reservoir conditions. Transp Porous Media 110 (1), 1–24.
Arganda-Carreras, I., Kaynig, V., Rueden, C., Eliceiri, K.W., Schindelin, J., Cardona, A., Sebastian Seung, H., 2017. Trainable weka segmentation: a machine learning tool for microscopy pixel classification. Bioinformatics 33 (15), 2424–2426.
Bartell, F.E., Osterhof, H.J., 1927. Determination of the wettability of a solid by a liquid. Industrial & Engineering Chemistry 19 (11), 1277–1280.
Blunt, M.J., 2001. Constraints on contact angles for multiple phases in thermodynamic equilibrium. J Colloid Interface Sci 239 (1), 281–282.
Blunt, M.J., 2017. Multiphase flow in permeable media: A Pore-Scale perspective. Cambridge University Press.
Blunt, M.J., Bijeljic, B., Dong, H., Gharbi, O., Iglauer, S., Mostaghimi, P., Paluszny, A., Pentland, C., 2013. Pore-scale imaging and modelling. Adv Water Resour 51, 197–216.
Brown, K., Schlüter, S., Sheppard, A., Wildenschild, D., 2014. On the challenges of measuring interfacial characteristics of three-phase fluid flow with X-ray microtomography. J Microsc 253 (3), 171–182.
Buades, A., Coll, B., Morel, J.M., 2008. Nonlocal image and movie denoising. Int J Comput Vis 76 (2), 123–139.
Bultreys, T., Hoorebeke, L.V., Cnudde, V., 2015. Multi-scale, micro-computed tomography-based pore network models to simulate drainage in heterogeneous rocks. Adv Water Resour 78, 36–49.
Bultreys, T., Lin, Q., Gao, Y., Raeini, A.Q., AlRatrout, A., Bijeljic, B., Blunt, M.J., 2018. Validating model predictions of pore-scale fluid distributions during two-phase flow in rocks. Phys Rev E 053104 (May).
Di Carlo, D.A., Sahni, A., Blunt, M.J., Stanford, U., 2000. Three-phase relative permeability and mixed-wet sandpacks. SPE J. 5 (1), 27–30.
Dong, H., Blunt, M.J., 2009. Pore-network extraction from micro-computerized-tomography images. Phys Rev E 80 (3), 036307.
Feali, M., Pinczewski, W.V., Cinar, Y., Arns, C.H., Arns, J.-y., South, N., Turner, M., 2012. Qualitative and quantitative analyses of the three-Phase distribution of oil , water , and gas in bentheimer sandstone by use of micro-CT imaging. SPE Reserv Eval Eng 15 (January), 706–711.
Figuera, L., Al-Basry, A., Al-Hammadi, K., Al-Yafei, A., Sakaria, D., Tanakov, M., 2014. Complex phased development for CO2 EOR in oil carbonate reservoir, abu dhabi onshore. SPE Abu Dhabi International Petroleum Exhibition and Conference, 10–13 November, Abu Dhabi, UAE. SPE-171967-MS.
Global CCS institute, 2016. The Global Status of CCS 2016 Summary Report. Technical Report.
Herring, A.L., Middleton, J., Walsh, R., Kingston, A., Sheppard, A., 2017. Flow rate impacts on capillary pressure and interface curvature of connected and disconnected fluid phases during multiphase flow in sandstone. Adv Water Resour 107, 460–469.
Hildebrand, T., Ruegsegger, P., 1997. A new method for the model-independent assessment of thickness in three-dimensional images. J Microsc 185 (1), 67–75.
IEA, 2017. Energy Technology Perspectives 2017 - Executive Summary.
Iglauer, S., Paluszny, A., Blunt, M.J., 2013. Simultaneous oil recovery and residual gas storage: a pore-level analysis using in situ X-ray micro-tomography. Fuel 103, 905–914.
Iglauer, S., Sarmadivaleh, M., Lebedev, M., Ferno, M., 2014. Influence of wettability on residual gas trapping and enhanced oil recovery in three-Phase flow : a pore-Scale analysis using micro-Computed tomography 41353 (October 2015), 1–14.
Jafari, M., Jung, J., 2017. Direct measurement of static and dynamic contact angles using a random micromodel considering geological CO2 sequestration. Sustainability 9 (12), 2352.
Jones, A.C., Arns, C.H., Sheppard, A.P., Hutmacher, D.W., Milthorpe, B.K., Knackstedt, M.A., 2007. Assessment of bone ingrowth into porous biomaterials using micro-CT. Biomaterials 28 (15), 2491–2504.
Kamaljit, S., Branko, B., J., B.M., 2016. Imaging of oil layers, curvature and contact angle in a mixed-wet and a water-wet carbonate rock. Water Resour Res 52 (3), 1716–1728.
Keller, A., Blunt, M.J., Roberts, A., 1997. Micromodel observation of the role of oil layers in three-Phase flow. Transp Porous Media 26 (3), 277–297.
Khishvand, M., Alizadeh, A.H., Piri, M., 2016. In-Situ characterization of wettability and pore-Scale dzisplacements during two- and three-Phase flow in natural porous media. Adv Water Resour 97 (11), 279–298.
Kolster, C., Masnadi, M.S., Krevor, S., Mac Dowell, N., Brandt, A.R., 2017. Co2 enhanced oil recovery: a catalyst for gigatonne-scale carbon capture and storage deployment? Energy Environ Sci 10, 2594–2608.
Leung, D.Y., Caramanna, G., Maroto-Valer, M.M., 2014. An overview of current status of carbon dioxide capture and storage technologies. Renew Sustain Energy Rev 39, 426–443.
Moghadasi, L., Guadagnini, A., Inzoli, F., Bartosek, M., Renna, D., 2016. Characterization of two- and three-phase relative permeability of water-wet porous media through X-Ray saturation measurements. J Petrol Sci Eng 145, 453–463.
Nakamura, K., Kikumoto, M., 2014. Modeling water - NAPL - air three-phase capillary behavior in soils. Soils and Foundations 54 (6), 1225–1235.

Oak, M., Baker, L.E., Thomas, D.C., 1990. Three-Phase relative permeability of berea sandstone. J Petrol Technol 42 (8), 1054–1061.
Oren, P.E., Billiotte, J., Pinczewski, W.V., 1992. Mobilization of waterflood residual oil by gas injection for water-wet conditions. SPE Form Eval 7, 70–78.
Piri, M., Blunt, M.J., 2005. Three-dimensional mixed-wet random pore-scale network modeling of two- and three-phase flow in porous media. i. model description. Phys Rev E 71, 026301.
Rabbani, H.S., Joekar-Niasar, V., Pak, T., Shokri, N., 2017. New insights on the complex dynamics of two-phase flow in porous media under intermediate-wet conditions. Sci Rep 7 (1), 4584.
Raeini, A.Q., Bijeljic, B., Blunt, M.J., 2017. Generalized network modeling: network extraction as a coarse-scale discretization of the void space of porous media. Phys Rev E 96 (1), 013312.
Ranaee, E., Porta, G.M., Riva, M., Blunt, M.J., Guadagnini, A., 2015. Prediction of three--phase oil relative permeability through a sigmoid-based model. J Petrol Sci Eng 126, 190–200.
Ranaee, E., Riva, M., Porta, G.M., Guadagnini, A., 2016. Comparative assessment of three--phase oil relative permeability models. Water Resour Res 52 (7), 5341–5356.
Reynolds, C.A., Menke, H., Andrew, M., Blunt, M.J., Krevor, S., 2017. Dynamic fluid connectivity during steady-state multiphase flow in a sandstone.. Proc Natl Acad Sci USA 114 (31), 8187–8192.
Scanziani, A., 2018. Water-wet three-phase flow micro-ct tomograms. Digital Rocks Portal. Available at https://www.digitalrocksportal.org/projects/167, doi:10.17612/P7HT11.
Scanziani, A., Singh, K., Blunt, M.J., Guadagnini, A., 2017. Automatic method for estimation of in situ effective contact angle from X-ray micro tomography images of two-phase flow in porous media. J Colloid Interface Sci 496, 51–59.
Schlüter, S., Berg, S., Rücker, M., Armstrong, R.T., Vogel, H.J., Hilfer, R., Wildenschild, D., 2016. Pore-scale displacement mechanisms as a source of hysteresis for two-phase flow in porous media. Water Resour Res 52 (3), 2194–2205.
Schlüter, S., Sheppard, A., Brown, K., Wildenschild, D., 2014. Image processing of multiphase images obtained via X-ray microtomography: A review.
Singh, K., Menke, H., Andrew, M., Lin, Q., Rau, C., Blunt, M.J., Bijeljic, B., 2017. Dynamics of snap-off and pore-filling events during two-phase fluid flow in permeable media. Sci Rep 7 (1), 5192.
Sohrabi, M., Danesh, A., Tehrani, D.H., Jamiolahmady, M., 2008. Microscopic mechanisms of oil recovery by near-miscible gas injection. Transp Porous Media 72 (3), 351–367.
Sohrabi, M., Tehrani, D., Danesh, A., Henderson, G., 2004. Visualization of oil recovery by water-Alternating-Gas injection using high-Pressure micromodels. SPE J 9 (3), 290–301.
Sorbie, K.S., Dijke, M.I.J.V., 2010. The mechanism of oil recovery by water-Alternating–Gas injection at near-Miscible conditions in mixed wet systems. SPE Improved Oil Recovery Symposium, 24–28 April, Tulsa, Oklahoma, USA. SPE 129837.
National Institute of Standards and Technology, 201. XCOM photon cross sections database. Available at https://www.nist.gov/pml/xcom-photon-cross-sections-database.
Statoil, 2017. Energy perspectives. Long-term macro and market outlook 2017. Available at https://www.statoil.com/content/dam/statoil/documents/energy-perspectives/energy-perspectives-2017-v2.pdf.
Tanino, Y., Blunt, M.J., 2012. Capillary trapping in sandstones and carbonates: dependence on pore structure. Water Resour Res 48 (8), 1–13.
Van Dijke, M.I.J., Sorbie, K., Sohrabi, M., Danesh, A., 2004. Three-Phase flow WAG processes in mixed-Wet porous media: pore-Scale network simulations and comparison with water-Wet micromodel experiment. SPE J 9 (1), 57–66.
Van Dijke, M.I.J., Sorbie, K.S., 2002. Pore-scale network model for three-phase flow in mixed-wet porous media. Phys Rev E 66, 046302.
Van Dijke, M.I.J., Sorbie, K.S., Sohrabi, M., Danesh, A., 2006. Simulation of WAG floods in an oil-wet micromodel using a 2-D pore-scale network model. Journal of Petroleum Science and Engineering 52, 71–86.
Vizika, O., Lombard, J.-M., 1996. Wettability and spreading: two key parameters in oil recovery with three-Phase gravity drainage. SPE Reservoir Eng 11 (1), 54–60.
Zolfaghari, A., Piri, M., 2017. Pore-scale network modeling of three-phase flow based on thermodynamically consistent threshold capillary pressures. i. cusp formation and collapse. Transp Porous Media 116 (3), 1093–1137.
Zolfaghari, A., Piri, M., 2017. Pore-scale network modeling of three-phase flow based on thermodynamically consistent threshold capillary pressures. ii. results. Transp Porous Media 116 (3), 1139–1165.